



HAL
open science

Retrieval of cloud properties using CALIPSO Imaging Infrared Radiometer. Part II: effective diameter and ice water path

Anne Garnier, Jacques Pelon, Philippe Dubuisson, Ping Yang, Michaël Faivre, Olivier Chomette, Nicolas Pascal, Pat Lucker, Tim Murray

► To cite this version:

Anne Garnier, Jacques Pelon, Philippe Dubuisson, Ping Yang, Michaël Faivre, et al.. Retrieval of cloud properties using CALIPSO Imaging Infrared Radiometer. Part II: effective diameter and ice water path. *Journal of Applied Meteorology and Climatology*, 2013, 52 (11), pp.2582-2599. 10.1175/JAMC-D-12-0328.1 . hal-00846790

HAL Id: hal-00846790

<https://hal.science/hal-00846790>

Submitted on 8 Dec 2020

HAL is a multi-disciplinary open access archive for the deposit and dissemination of scientific research documents, whether they are published or not. The documents may come from teaching and research institutions in France or abroad, or from public or private research centers.

L'archive ouverte pluridisciplinaire **HAL**, est destinée au dépôt et à la diffusion de documents scientifiques de niveau recherche, publiés ou non, émanant des établissements d'enseignement et de recherche français ou étrangers, des laboratoires publics ou privés.

Retrieval of Cloud Properties Using *CALIPSO* Imaging Infrared Radiometer. Part II: Effective Diameter and Ice Water Path

ANNE GARNIER,^{*,+,#} JACQUES PELON,[#] PHILIPPE DUBUISSON,[@] PING YANG,[&] MICHAËL FAIVRE,[#]
OLIVIER CHOMETTE,^{**} NICOLAS PASCAL,⁺⁺ PAT LUCKER,^{*,+} AND TIM MURRAY^{*,+}

^{*} *Science Systems and Applications, Inc., Hampton, Virginia*

⁺ *NASA Langley Research Center, Hampton, Virginia*

[#] *Laboratoire Atmosphères, Milieux, Observations Spatiales, UPMC-UVSQ-CNRS, Paris, France*

[@] *Laboratoire d'Optique Atmosphérique, Université de Lille 1, Lille, France*

[&] *Department of Atmospheric Sciences, Texas A&M University, College Station, Texas*

^{**} *Laboratoire de Météorologie Dynamique, École Polytechnique, Palaiseau, France*

⁺⁺ *Hygeos, Cloud–Aerosol–Water–Radiation Interactions (ICARE), Lille, France*

(Manuscript received 7 December 2012, in final form 7 June 2013)

ABSTRACT

This paper describes the version-3 level-2 operational analysis of the Imaging Infrared Radiometer (IIR) data collected in the framework of the *Cloud–Aerosol Lidar and Infrared Pathfinder Satellite Observations (CALIPSO)* mission to retrieve cirrus cloud effective diameter and ice water path in synergy with the Cloud–Aerosol Lidar with Orthogonal Polarization (CALIOP) collocated observations. The analysis uses a multi-sensor split-window technique relying on the concept of microphysical index applied to the two pairs of channels (12.05, 10.6 μm) and (12.05, 8.65 μm) to retrieve cirrus microphysical properties (effective diameter, ice water path) at 1-km pixel resolution. Retrievals are performed for three crystal families selected from precomputed lookup tables identified as representative of the main relationships between the microphysical indices. The uncertainties in the microphysical indices are detailed and quantified, and the impact on the retrievals is simulated. The possible biases have been assessed through consistency checks that are based on effective emissivity difference. It has been shown that particle effective diameters of single-layered cirrus clouds can be retrieved, for the first time, down to effective emissivities close to 0.05 when accurate measured background radiances can be used and up to 0.95 over ocean and land, as well as over low opaque clouds. The retrieval of the ice water path from the IIR effective optical depth and the effective diameter is discussed. Taking advantage of the cloud boundaries retrieved by CALIOP, an IIR power-law relationship between ice water content and extinction is established for four temperature ranges and shown to be consistent with previous results on average for the chosen dataset.

1. Introduction

Microphysical properties of ice clouds are important to radiation budget analysis but are still difficult to retrieve accurately because of their natural variability, their radiative properties, and the frequent multilayered cloud structure. Ice crystal effective diameters and ice water path retrievals have been performed from spaceborne passive instruments such as the Moderate Resolution Imaging Spectroradiometer (MODIS) on *Terra* and *Aqua* (Platnick et al. 2003), Meteosat Second

Generation–Spinning Enhanced Visible and Infrared Imager (MSG-SEVIRI; Bugliaro et al. 2011), and Advanced Very High Resolution Radiometer (AVHRR; Roebeling et al. 2006), mostly using a combination of observations in the visible and near-infrared spectral domain (Nakajima and King 1990). Retrievals have also been performed in the 8–12- μm atmospheric window from a number of spectral bands of various resolutions, using the split-window technique (Inoue 1985). The technique relies on the spectral signature of cirrus clouds in this domain, which is related to the varying absorption by ice (Warren 1984; Warren and Brandt 2008), the cirrus microphysical properties, and meteorological and surface parameters. The spectral signature has been analyzed in terms of interchannel brightness temperature

Corresponding author address: Anne Garnier, SSAI, 1 Enterprise Parkway, Suite 200, Hampton, VA 23666.
E-mail: anne.garnier@latmos.ipsl.fr

differences (BTD) by using radiative transfer models to simulate the observations and ultimately retrieve the cloud optical and microphysical properties from daytime or nighttime operation (Ackerman et al. 1990, 1995; Duda et al. 1998; Chiriaco et al. 2004; Yue et al. 2007; Wang et al. 2011). The cirrus spectral signature can also be analyzed in terms of interchannel effective emissivity differences as applied to the high spectral resolution Television Infrared Observation Satellite (TIROS) Operational Vertical Sounder (TOVS; Stubenrauch et al. 1999; Rädcl et al. 2003) and Atmospheric Infrared Sounder (AIRS; Guignard et al. 2012, hereinafter Gu12). A third approach based on the concept of microphysical index has also been proposed by Parol et al. (1991) to minimize the contribution of cloud optical depth in the ice cloud spectral signature analysis. The microphysical index was originally defined as the ratio of the effective optical depths in the AVHRR channels centered at 12 and 11 μm . This concept, further tested by Giraud et al. (1997) using radiometric data only, has been applied to the analysis of our data for the *Cloud–Aerosol Lidar and Infrared Pathfinder Satellite Observations (CALIPSO)* mission. It has also been considered for existing and future datasets (Heidinger and Pavolonis 2009; Heidinger et al. 2010; Pavolonis 2010). The representativeness and accuracy of the retrievals in the thermal infrared are conditioned by the scene identification. Using passive sensors, the cloud altitude is derived from multispectral analysis and most accurately by the CO_2 slicing method (Stubenrauch et al. 1999; Rädcl et al. 2003). Lidar and radar active sensors recently implemented in the A-Train offer improved cloud boundary retrievals (Stubenrauch et al. 2010).

This paper describes the operational retrieval of ice cloud particle effective diameter and cloud ice water path from the *CALIPSO* Imaging Infrared Radiometer (IIR) by taking advantage of the range-resolved inputs provided by the perfectly collocated *CALIPSO* lidar [Cloud–Aerosol Lidar with Orthogonal Polarization (CALIOP)] observations. The three IIR channels are centered at 8.65, 10.6, and 12.05 μm , with medium spectral resolutions of 0.6–1 μm (Corlay et al. 2000). The onboard calibrated radiances have been validated by comparison with airborne observations (Sourdeval et al. 2012). The IIR level-2 operational algorithm uses the concept of microphysical index applied to the pairs of channels (12.05, 10.6) and (12.05, 8.65). Those indices can be primarily related to the ice crystal effective diameter and shape through lookup tables (LUT) assuming that the ice crystals can be modeled. They are computed from the effective emissivity in each channel, as detailed in the first part of this paper (Garnier et al.

2012, hereinafter G1). This approach is being used for the first time to operationally derive ice crystal microphysical properties. An overview of the analysis is provided in section 2, followed by the presentation of the effective diameter retrievals in section 3. The sources of uncertainties are described and illustrated in section 4. Results are shown and discussed in section 5 before ending with conclusions in section 6.

2. Microphysical properties analysis

a. Definitions

To retrieve cloud microphysical properties from remote sensing techniques, we first need to adopt a procedure to link these properties to the optical ones. The ice water content $\text{IWC}(z)$ profile is obtained from the local volume distribution $V(D, L, z)$ of the ice crystals of width D and length L , at a given altitude z in the cloud as

$$\text{IWC}(z) = \rho_i \int_{D,L} V(D, L, z) n(D, L, z) dD dL, \quad (1)$$

where ρ_i is the density of solid ice (approximately $9.17 \times 10^2 \text{ kg m}^{-3}$), and $n(D, L, z)$ is the size distribution as a function of altitude. The effective diameter D_e is defined from the ratio of the volume to the projected area over the whole size distribution, and for nonspherical particles, over the various shapes. Mitchell (2002) showed that by analogy with spheres, and by using the projected area-to-extinction relationship, IWC and the extinction coefficient α can be linked through the effective diameter D_e as

$$\text{IWC}(z) = \frac{2}{3} \rho_i \times \frac{\alpha(z)}{Q_e} \times D_e(z), \quad (2)$$

where Q_e is the extinction efficiency representing the entire size distribution, which, assuming that the cirrus particle sizes are much larger than the wavelength at which the extinction is retrieved, is equal to 2. Retrieving the ice water content from the extinction only, as for example derived from the CALIOP lidar, is thus equivalent to using a formulation of the effective diameter as a function of extinction and ice water content. The observations by McFarquhar et al. (2003, hereinafter McF03) shown in section 5 are reported for D_e defined from Eq. (2), which is proportional to the diameter D_{ge} defined in McF03 following Fu and Liou (1993) and Fu (1996), so that

$$D_e = \frac{9}{4\sqrt{3}} \times D_{\text{ge}} \approx 1.3 \times D_{\text{ge}}. \quad (3)$$

The ice water path (IWP) is the integral of IWC over the cloud layer. Looking for integral relationships over a whole cloud layer is more complicated, as the properties are expected to vary from bottom to top. The relationship between IWP, optical depth τ , and D_e is usually given by

$$\text{IWP} = A_s \frac{\tau}{D_e + B_s} D_e, \quad (4)$$

where the coefficients A_s and B_s can be derived from observations or from theoretical simulations and depend on the shape (Ebert and Curry 1992; Mitchell 2002; Heymsfield et al. 2003; Dubuisson et al. 2008). In this work, a simplified formulation between the IWP, the effective optical depth at $12.05 \mu\text{m}$ OD_{eff} , and the integrated effective diameter $\langle D_e \rangle$ is derived using Eq. (2), assuming $Q_e = 2$, such as

$$\text{IWP} = \frac{1}{3} \rho_i (2 \times \text{OD}_{\text{eff}}) \langle D_e \rangle 10^{-3}, \quad (5)$$

as proposed by Stephens (1978), where D_e and IWP are in micrometers and grams per meter squared, respectively. It is to be noticed that the extinction efficiencies Q_e derived by Fu et al. (1998) in the infrared using finite-difference time domain (FDTD) calculations are slightly larger than 2. In our simplified expression, the extinction optical depth at $12.05 \mu\text{m}$ is taken equal to 2 times the effective optical depth inferred from the effective emissivity (see G1 for details), which assumes that OD_{eff} is purely an absorption optical depth, with no contribution from multiple scattering, and that the scattering albedo is equal to 0.5 over the full range of sizes. This simplification biases the IWP by about +10% for $D_e = 20 \mu\text{m}$ and $\pm 5\%$ for $D_e > 30 \mu\text{m}$. Comparisons with the expression given by Eq. (4) and used by Dubuisson et al. (2008) show that our IWP derived from Eq. (5) is overall larger by 15%–20%. On the other hand, it is by 10%–25% smaller than simulated by Gui12, who use different crystal optical properties.

b. IIR data analysis

Extending the approach developed in Parol et al. (1991), the IIR level-2 microphysical algorithm first computes the two effective microphysical index pairs

$$\beta_{\text{eff}12/10} = \ln(1 - \varepsilon_{\text{eff},12}) / \ln(1 - \varepsilon_{\text{eff},10}) \quad (6a)$$

and

$$\beta_{\text{eff}12/08} = \ln(1 - \varepsilon_{\text{eff},12}) / \ln(1 - \varepsilon_{\text{eff},08}), \quad (6b)$$

where $\varepsilon_{\text{eff},08}$, $\varepsilon_{\text{eff},10}$, and $\varepsilon_{\text{eff},12}$ are the effective emissivities retrieved at 8.65, 10.6, and $12.05 \mu\text{m}$, respectively.

Then, LUTs are screened to extract the effective diameters derived from the $\beta_{\text{eff}12/10}$ and the $\beta_{\text{eff}12/08}$ microphysical index pairs for each selected crystal model. The LUTs are built offline using the Fast Discrete Ordinate Method (FASDOM) radiative transfer model (Dubuisson et al. 2005) and crystal models selected in a precomputed database (Yang et al. 2005). In this version of the algorithm, a simple approach has been chosen by limiting the number of crystal models and by considering monodisperse size distributions, as discussed in section 3. The crystal model providing the best agreement between the 12/08 ($D_{e12/08}$) and 12/10 ($D_{e12/10}$) diameters is retained. The effective diameter D_e is taken as the mean of $D_{e12/08}$ and $D_{e12/10}$, whereas the quantity defined as $(D_{e12/08} - D_{e12/10})/2$ represents the disagreement between both diameters. Finally, the algorithm provides an estimate for the cloud ice water path determined from its effective optical depth at $12.05 \mu\text{m}$ and D_e . The three parameters OD_{eff} , D_e , and IWP are retrieved sequentially, first under the lidar track and then spread to the IIR swath using homogeneity criteria based on radiative equivalence as described in G1.

3. Retrieval of effective diameters

a. The microphysical indices

The effective microphysical indices $\beta_{\text{eff}12/10}$ and $\beta_{\text{eff}12/08}$ are ratios of the respective effective optical depths. The relationship between the effective emissivities could also have been defined as in other studies through their differences, that is, $\Delta\varepsilon_{12-10} = \varepsilon_{\text{eff},12} - \varepsilon_{\text{eff},10}$ and $\Delta\varepsilon_{12-08} = \varepsilon_{\text{eff},12} - \varepsilon_{\text{eff},08}$. As the emissivity approach is closer to the BTM analysis first used in the split-window and more familiar, both approaches are discussed in parallel. As an illustration, Fig. 1 shows the variation of $\Delta\varepsilon_{12-10}$ (Fig. 1a) and $\beta_{\text{eff}12/10}$ (Fig. 1b) with $\varepsilon_{\text{eff},12}$ computed using the FASDOM model for a cloud composed of solid columns of effective diameters between 11 and $80 \mu\text{m}$. Figures 2a and 2b show the same results for the 12/08 pair. The computations assume an isothermal cloud, simulating the cloud-layer equivalent temperature inferred from the CALIOP centroid altitude of the 532-nm attenuated backscatter coefficient in the operational algorithm (see G1). It is seen that the dependence on emissivity almost disappears in the microphysical index approach.

Superimposed in Fig. 1b (dashed lines) are the approximate values of $\beta_{\text{eff}12/10}$ defined by Parol et al. (1991) as

$$\beta_{\text{proxy}12/10} = [(1 - \omega_{12}g_{12})Q_{12}] / [(1 - \omega_{10}g_{10})Q_{10}], \quad (7)$$

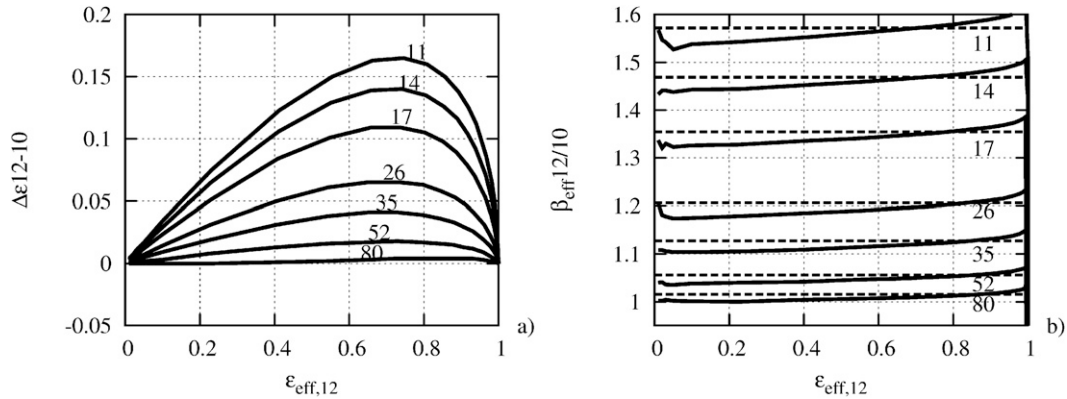


FIG. 1. (a) The $\Delta\epsilon_{12-10}$ vs $\epsilon_{\text{eff},12}$ and (b) $\beta_{\text{eff}12/10}$ vs $\epsilon_{\text{eff},12}$ for an ice cloud composed of solid columns of effective diameters 11, 14, 17, 26, 35, 52, and 80 μm . The dashed lines in (b) are approximate values after Parol et al. (1991).

where ω_k is the single-scattering albedo, g_k is the asymmetry factor, and Q_k is the extinction efficiency in the IIR channels 12.05 μm (noted $k = 12$) and 10.6 μm ($k = 10$). Similarly, superimposed in Fig. 2b is $\beta_{\text{proxy}12/08}$ defined from Eq. (7) for the 12/08 pair. The microphysical indices are found in good agreement with their respective approximate value; more noticeably for the 12/10 pair (Fig. 1b). The differences are mostly due to the full computation of the contribution of the multiple scattering, which induces a weak sensitivity to the effective emissivity, more importantly for diameters smaller than 20 μm and for the 12/08 pair. To account for the residual variation with the effective emissivity, the IIR analysis uses a set of LUTs chosen so that $\beta_{\text{eff}12/k}$ is sampled with a step of the order of the expected random noise. Nevertheless, these simulations show that the approximate values, independent of the effective emissivity, are relevant for quick studies such as comparisons of crystal models.

The sensitivity of the split-window technique decreases for optically very thin and very thick cirrus clouds, with effective emissivity differences (Figs. 1a and 2a) tending

to 0, allowing consistency checks, as shown in section 4. The varying sensitivity of the method with $\epsilon_{\text{eff},12}$ propagates to the uncertainties in the microphysical indices, as discussed in section 4.

b. Crystal models and size retrievals

The relationship between the microphysical indices $\beta_{\text{eff}12/10}$ and $\beta_{\text{eff}12/08}$ derived from the IIR analysis is used to determine the family of crystal models that agrees the best with the observations. The effective diameter D_e is then retrieved from a reference model chosen as representative of the selected family. The choice of the reference models used in the algorithm is presented and discussed in the following subsections.

1) CRYSTAL SHAPE

The seven models available in the precomputed database have been compared in terms of microphysical indices using Eq. (7) and assuming a monodisperse distribution. Results are plotted in Figs. 3a and 3b showing $\beta_{\text{eff}12/10}$ against D_e and $\beta_{\text{eff}12/08}$, respectively. Figure 3a shows more directly than Fig. 1b that the sensitivity of

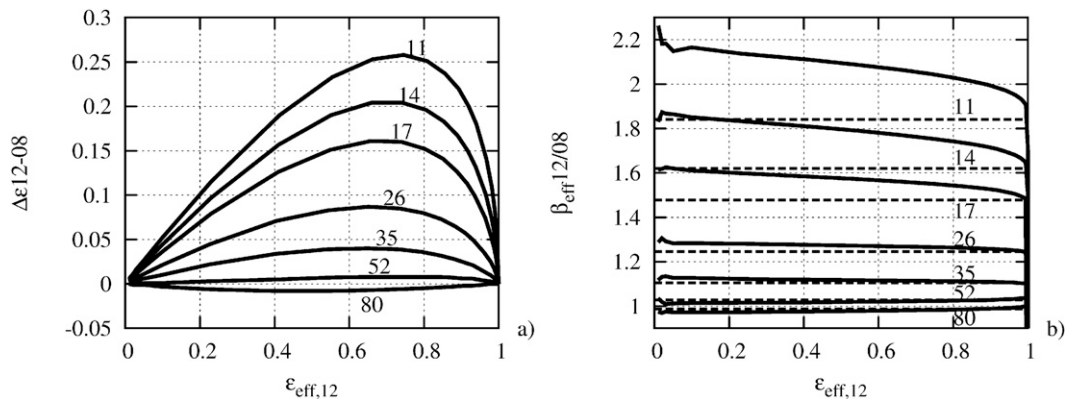


FIG. 2. As in Fig. 1, but for $\Delta\epsilon_{12-08}$ and $\beta_{\text{eff}12/08}$ and a different vertical scale.

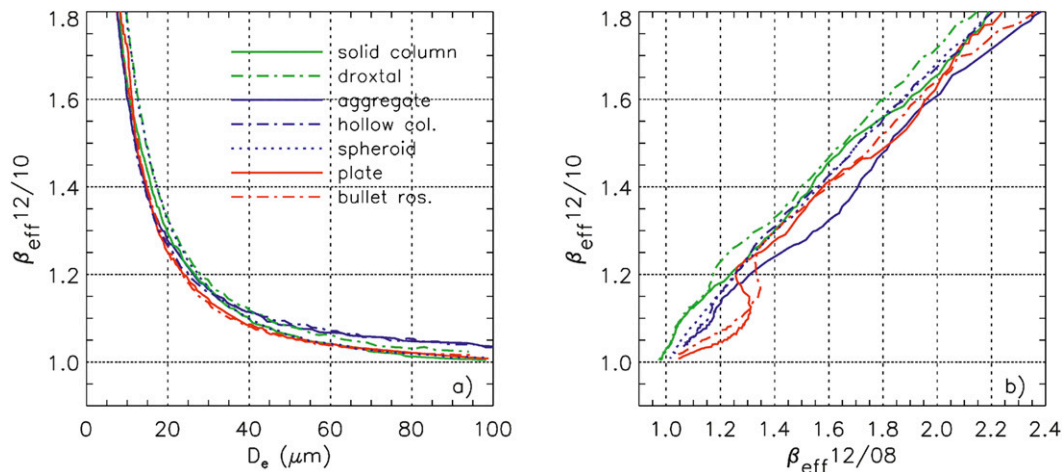


FIG. 3. The (a) $\beta_{\text{eff}}^{12/10}$ vs effective diameter D_e and (b) $\beta_{\text{eff}}^{12/10}$ vs $\beta_{\text{eff}}^{12/08}$ for seven of P. Yang's crystal models.

the method decreases as the effective diameter increases [the derivative of $\beta_{\text{eff}}(D_e)$ is about 10 times larger at $10 \mu\text{m}$ than at $50 \mu\text{m}$]. It also shows that the sensitivity to the crystal model increases at large diameters. As seen in Fig. 3b, the models can be better distinguished through the relationship between $\beta_{\text{eff}}^{12/10}$ and $\beta_{\text{eff}}^{12/08}$. Keeping in mind the expected random error on the retrieved microphysical indices estimated at ± 0.025 in the best conditions (see section 4), three main families of relationships can be identified, especially for $\beta_{\text{eff}}^{12/10}$ smaller than 1.2 (or D_e larger than about $25 \mu\text{m}$), with differences in $\beta_{\text{eff}}^{12/08}$ of about 0.1. They are a) aggregates, hollow columns, and spheroids (blue); b) bullet rosettes and plates (red); and c) solid columns and droxtals (green). Values of D_e associated with given values of $\beta_{\text{eff}}^{12/10}$ are listed in Table 1 for each model in each family (a, b, and c). One model per family is selected for the operational algorithm. Aggregates, chosen in family a, are similar to hollow columns in Table 1, and characterized by the largest $\beta_{\text{eff}}^{12/08}$ to $\beta_{\text{eff}}^{12/10}$ ratio for $\beta_{\text{eff}}^{12/10}$ larger than 1.3 (Fig. 3b). In family b, we choose plates, whose radiative signature in terms of β_{eff} is very close to bullet rosettes. In family c, solid columns

are selected, as they exhibit the smallest values of β_{eff} at large diameter. We recognize that spheroids and droxtals are not well represented for $\beta_{\text{eff}}^{12/10}$ around 1.05, in a range of values where the sensitivity of the method is anyways limited when compared to the random errors. However, as emphasized in Dubuisson et al. (2008), the shape can be identified as a parameter with significant impact on the radiative signature. The crystal model selection within a family could be refined by accounting for temperature. For example, in family b, plates are more frequent at temperatures between -10° and -20°C than bullet rosettes (Pruppacher and Klett 1997).

2) SIZE DISTRIBUTION

As the size distribution (and the crystal models) may vary between cloud types, a simple approach was chosen in this version of the operational analysis. Indeed, the primary focus has been given to the observations and to an unbiased retrieval of the microphysical indices (see section 4) required to correctly identify the crystal family. Thus, for each family, the microphysical indices are computed for the selected reference model assuming a monodisperse size distribution. They have been compared

TABLE 1. Values of the effective diameters D_e (μm) associated with given values of $\beta_{\text{eff}}^{12/10}$ for each model in each family for a monodisperse size distribution.

$\beta_{\text{eff}}^{12/10}$	Family a			Family b		Family c	
	Aggregate	Hollow column	Spheroid	Plate	Bullet rosette	Solid column	Droxtal
1.6	10.1	10	12.6	11	10.6	10.5	12.8
1.2	26.2	24.7	27.3	24.1	23.5	26.6	28
1.1	43.2	44.5	40	36.1	35.3	39.6	43.9
1.05	78	74.6	55	51.6	54	53.4	64.8
1.0	—	—	—	103	121	112	165

TABLE 2. Values of the effective diameters D_e (μm) associated with given values of $\beta_{\text{eff}12/10}$ for two monomodal distributions (small and large mode) for aggregates, plates, and solid columns selected as representative of the families a, b, and c, respectively.

$\beta_{\text{eff}12/10}$	Family a		Family b		Family c	
	Small mode	Large mode	Small mode	Large mode	Small mode	Large mode
1.6	10.4	10.5	11	11.6	11.1	11.7
1.2	27	30.3	24.4	25.9	27	31.3
1.1	44.5	54	37.8	40	40.5	47.3
1.05	76	98.3	52.7	56.3	56	63.4
1.0	—	—	103	112	112	117

as in Dubuisson et al. (2008) with those obtained for two monomodal distributions simulating two extreme cases. These cases are small particles in young cirrus and large particles produced by aggregation. Computations show that the size distribution does not change the relationships between $\beta_{\text{eff}12/10}$ and $\beta_{\text{eff}12/08}$ and that consequently it does not impact the selection of the crystal family. Values of D_e associated with given values of $\beta_{\text{eff}12/10}$ for the two monomodal distributions (small and large mode) are reported in Table 2 for the three models selected earlier. No significant differences are found for the small mode, whereas the spectral response is slightly different for the large mode. For solid columns and aggregates, effective diameters derived assuming a pure large mode are larger by 12%–15% at $D_e = 30 \mu\text{m}$ and 20% at $D_e = 45 \mu\text{m}$, compatible with results reported from other work (Rädcl et al. 2003). This is about the same order of magnitude as other error sources as shown in the next section, where the sources of uncertainties (random error and possible biases) and their impact on the microphysics retrievals are discussed.

4. Sensitivity analysis and uncertainties

a. Microphysical indices

The effective microphysical indices, $\beta_{\text{eff}12/k}$, are a function of the effective emissivities $\varepsilon_{\text{eff},12}$ and $\varepsilon_{\text{eff},k}$ at $12.05 \mu\text{m}$ and in channel k . We discuss first the sources of uncertainties in the difference $\Delta\varepsilon12-k = \varepsilon_{\text{eff},12} - \varepsilon_{\text{eff},k}$, and then present their impact on $\beta_{\text{eff}12/k}$.

For each channel k , the effective emissivity $\varepsilon_{\text{eff},k}$ is retrieved as described in G1:

$$\varepsilon_{\text{eff},k} = \frac{R_k - R_{k,\text{BG}}}{B_k(T_c, Z_c) - R_{k,\text{BG}}}. \quad (8)$$

In Eq. (8), R_k is the calibrated radiance measured in channel k . The term $R_{k,\text{BG}}$ is the background radiance in channel k , that is, the radiance which would be observed in the absence of the studied cloud. Finally, $B_k(T_c, Z_c)$ is the radiance of a blackbody source located at the reference altitude Z_c of thermodynamic temperature T_c

retrieved from ancillary meteorological data. Upper-layer effective emissivities are retrieved for two main categories of background scenes, either the surface or an opaque layer. Furthermore, the background radiances are determined preferably from observations in neighboring pixels at a maximum distance of 100 km to minimize biases. If no suitable observations can be found, they are computed using the Fast-Calculation Radiative Transfer (FASRAD) model (Dubuisson et al. 2005) adapted to the IIR spectral functions and ancillary and atmospheric data. The FASRAD model is also used to compute the blackbody radiance assuming that the equivalent radiative altitude of the cloud Z_c is located at the centroid altitude of the cloud layer as determined by the CALIOP algorithm (see G1 for more details).

The errors on the interchannel differences in effective emissivity are computed using the formulation presented in G1. Thus, the uncertainty $d\Delta\varepsilon12-k$ in $\Delta\varepsilon12-k$ is composed of three terms associated with errors on the measurement, the background radiance, and the blackbody radiance for the channels 12 and k , respectively, as

$$d\Delta\varepsilon12-k_m = d\varepsilon m_{\text{eff},12} - d\varepsilon m_{\text{eff},k}, \quad (9a)$$

$$d\Delta\varepsilon12-k_{\text{BG}} = d\varepsilon \text{BG}_{\text{eff},12} - d\varepsilon \text{BG}_{\text{eff},k}, \quad (9b)$$

and

$$d\Delta\varepsilon12-k_{\text{BB}} = d\varepsilon \text{BB}_{\text{eff},12} - d\varepsilon \text{BB}_{\text{eff},k}. \quad (9c)$$

Similarly, the error $d\beta_{\text{eff}12/k}$ on the microphysical index $\beta_{\text{eff}12/k}$ is composed of three terms such as

$$d\beta_{\text{eff}12/k_x} = \left(\frac{\partial \beta_{\text{eff}12/k}}{\partial \varepsilon_{\text{eff},12}} \right) d\varepsilon x_{\text{eff},12} + \left(\frac{\partial \beta_{\text{eff}12/k}}{\partial \varepsilon_{\text{eff},k}} \right) d\varepsilon x_{\text{eff},k}, \quad (9d)$$

where the letter x refers either to m , BG , or BB as defined previously.

As in G1, the uncertainties are discussed in terms of equivalent brightness temperature uncertainties in the measured, background and blackbody radiances for the

TABLE 3. Random uncertainty estimates assuming background and blackbody radiances equivalent to 280 and 220 K, respectively. See text for details.

Error source	Parameter	$\epsilon_{\text{eff}} = 0.1$	$\epsilon_{\text{eff}} = 0.5$	$\epsilon_{\text{eff}} = 0.9$
Measurement	$d\Delta\epsilon_{12-k}$	0.0045	0.0035	0.0038
Background	$d\Delta\epsilon_{12-k}$	0.0042	0.0024	0.0006
Blackbody	$d\Delta\epsilon_{12-k}$	0.0007	0.0028	0.0046
All	$d\Delta\epsilon_{12-k}$	0.006	0.005	0.006
All	$d\beta_{\text{eff}12/k}$	0.08	0.025	0.03

$(\beta_{\text{eff}12/k} = 1.1)$

channels 12 and k named $dT_{m,12}$ and $dT_{m,k}$, $dT_{\text{BG},12}$ and $dT_{\text{BG},k}$, and $dT_{\text{BB},12}$ and $dT_{\text{BB},k}$, respectively. The effective emissivity uncertainties per kelvin of brightness temperature error for each contributor shown in G1 at $12.05\ \mu\text{m}$ are similar for the other channels. The approach to compute $d\Delta\epsilon_{12-k,x}$ for each contributor x is detailed in the next three subsections, followed by the simulation of the overall uncertainty in $d\Delta\epsilon_{12-k}$ and $\beta_{\text{eff}12/k}$. The simulations are for background and blackbody radiances corresponding to 280 and 220 K, respectively. The radiative contrast of 60 K is chosen to simulate conditions typically observed for single-layered cirrus clouds, as discussed in G1. Finally, the $\beta_{\text{eff}12/10}$ and $\beta_{\text{eff}12/08}$ indices are taken equal to 1.1, simulating cirrus clouds composed of solid columns of $38\text{-}\mu\text{m}$ effective diameter. Results are reported in Table 3.

1) ERROR ON THE RADIOMETRIC MEASUREMENTS

The error due to the measurement $d\Delta\epsilon_{12-k,m}$ [Eq. (9a)] is computed assuming that the uncertainties $dT_{m,12}$ and $dT_{m,k}$ in the brightness temperatures measured at $12.05\ \mu\text{m}$ and in channel k are not correlated. It is computed using the radiometric performances of typically $0.15\text{--}0.3\ \text{K}$ (see G1 for details) assessed by Centre National d'Études Spatiales (CNES).

2) ERRORS ON THE BACKGROUND RADIANCES

As seen in section 3, the difference in emissivity tends to zero (see Fig. 2a), and the microphysical index remains constant (see Fig. 2b), when the effective emissivity $\epsilon_{\text{eff},12}$ tends to 0. This condition is fulfilled when the background radiance $R_{k,\text{BG}}$ is correctly determined in each of the three IIR channels. This property is used to check for the existence of a bias in the determination of the background radiances by comparing the background brightness temperatures (BTs) determined from neighboring observations with those derived from the radiative transfer model, also reported in the IIR products.

The BT distributions of the differences between computations and observations are shown in Fig. 4 for the $12.05\text{-}\mu\text{m}$ channel (Fig. 4a), and for the 12–10 (Fig. 4b) and 12–08 (Fig. 4c) interchannel differences. The median value and standard deviation of the computed minus observed differences at $12.05\ \mu\text{m}$ are -0.05

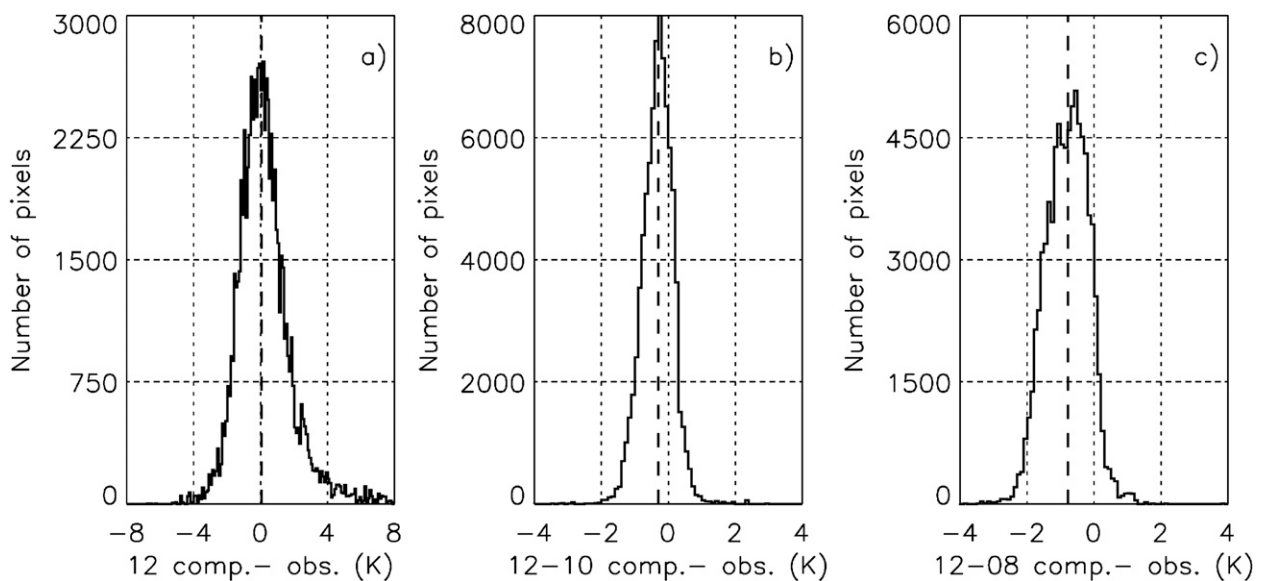


FIG. 4. Distribution of differences between computed and observed background brightness temperatures over ocean at (a) $12.05\ \mu\text{m}$ and for the (b) 12–10 and (c) 12–08 interchannel differences. Note that the horizontal scale in (a) is 2 times that of (b) and (c).

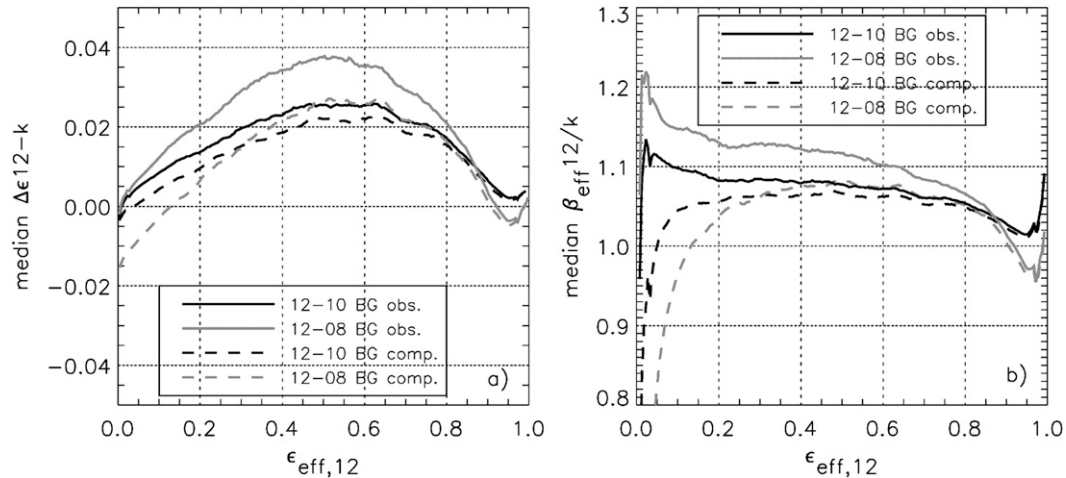


FIG. 5. (a) Median $\Delta\epsilon_{12-k}$ and (b) median $\beta_{\text{eff}12/k}$ (black: 12–10; gray: 12–08) against $\epsilon_{\text{eff},12}$ for single-layer high-altitude (>7 km) ice cirrus ($T_c < 233$ K) clouds (no aerosols), over ocean during January 2011. Background radiances are from neighboring observations (solid lines) or from computations (dashed lines).

and 1.7 K, respectively, showing no major bias in the retrieval at this wavelength. A small bias is however observed in the interchannel difference for 12–10 (-0.3 ± 0.4 K, slightly larger for 12–08 (-0.8 ± 0.6 K). This case study is for high-altitude (>7 km) single-layered cirrus clouds with no aerosols (type 21 and 40; see G1) of temperature T_c at the centroid altitude Z_c smaller than 233 K, over ocean during January 2011. The impact of these differences is clearly seen in Fig. 5 showing the median value of $\Delta\epsilon_{12-k}$ (Fig. 5a) and $\beta_{\text{eff}12/k}$ (Fig. 5b) versus $\epsilon_{\text{eff},12}$ for the background radiances retrieved from the neighboring observations (solid lines) and from the computations (dashed lines). For observed background radiances and $\epsilon_{\text{eff},12}$ tending to 0, the median values of $\Delta\epsilon_{12-08}$ and $\Delta\epsilon_{12-10}$ are -0.002 corresponding to residual biases of about -0.1 K. One can still see the existence of a small bias with a change of slope for $\epsilon_{\text{eff},12}$ smaller than 0.02, behavior that is better evidenced in the microphysical index approach (Fig. 5b). These residual biases are smaller than the radiometric measurement error of 0.14–0.18 K expected at warm brightness temperatures (see G1) for clear scenes over the ocean and are barely significant. As for computed background radiances, we find negative effective emissivity differences $d\Delta\epsilon_{12/10_BG} = -0.003$ and $d\Delta\epsilon_{12/08_BG} = -0.015$ for $\epsilon_{\text{eff},12}$ tending to 0 because of the biases shown in Figs. 4b and 4c. The difference between $\beta_{\text{eff}12/k}$ derived from computed and observed radiances shown in Fig. 5b is significant. As expected from Eq. (9b), the difference decreases with increasing $\epsilon_{\text{eff},12}$. In this example, it is 0.02 or more when $\epsilon_{\text{eff},12}$ is smaller than 0.4 for $\beta_{\text{eff}12/10}$, and $\epsilon_{\text{eff},12}$ smaller than 0.8 for $\beta_{\text{eff}12/08}$. We find that for $\epsilon_{\text{eff},12}$ from 0 to 0.1 (from 0.1 to 0.2),

100%–60% (60%–25%) of the values of $\beta_{\text{eff}12/k}$ derived from computations do not fall in the range of values expected from the LUTs (see Fig. 3), preventing the algorithm from attempting microphysics retrievals. Still, the algorithm is able to perform retrievals at larger emissivity, but the errors on $\beta_{\text{eff}12/k}$ bias the crystal model selection and the effective diameter retrievals toward too-large values in this case. On the contrary, when observed background radiances are used, microphysics retrievals are obtained in 50% of the cases for $\epsilon_{\text{eff},12} \sim 0$, with this percentage increasing to 75% for $\epsilon_{\text{eff},12} = 0.1$ and 90% for $\epsilon_{\text{eff},12} = 0.3$ as the random noise decreases, as discussed at the end of this section. The products derived when a clear-air observed reference is available are thus more accurate and should be considered preferentially in the analyses.

Similar studies have been performed to assess the relevance of the microphysical indices retrieved in case of semitransparent high-altitude (>7 km) single-layered cirrus ($T_c < 233$ K) clouds overlying a low (<7 km) opaque cloud (type 31; see G1). The results are shown in Figs. 6 and 7 similarly as in Figs. 4 and 5, respectively. The only difference is that the background radiance is not taken as corresponding to the surface, but to the underlying low opaque cloud. Here, the median value of the computed minus observed BT differences seen in Fig. 6 is rather large (2.1 ± 2.2) K at $12.05 \mu\text{m}$, consistent with results discussed in G1. By contrast, the interchannel differences remain comparable to the clear-air case, with even smaller discrepancies in absolute value equal to (0.2 ± 0.6) K for 12–10 and (-0.3 ± 0.6) K for 12–08. We observe a 0.5-K difference between both interchannel BTDs as for clear air. For computed

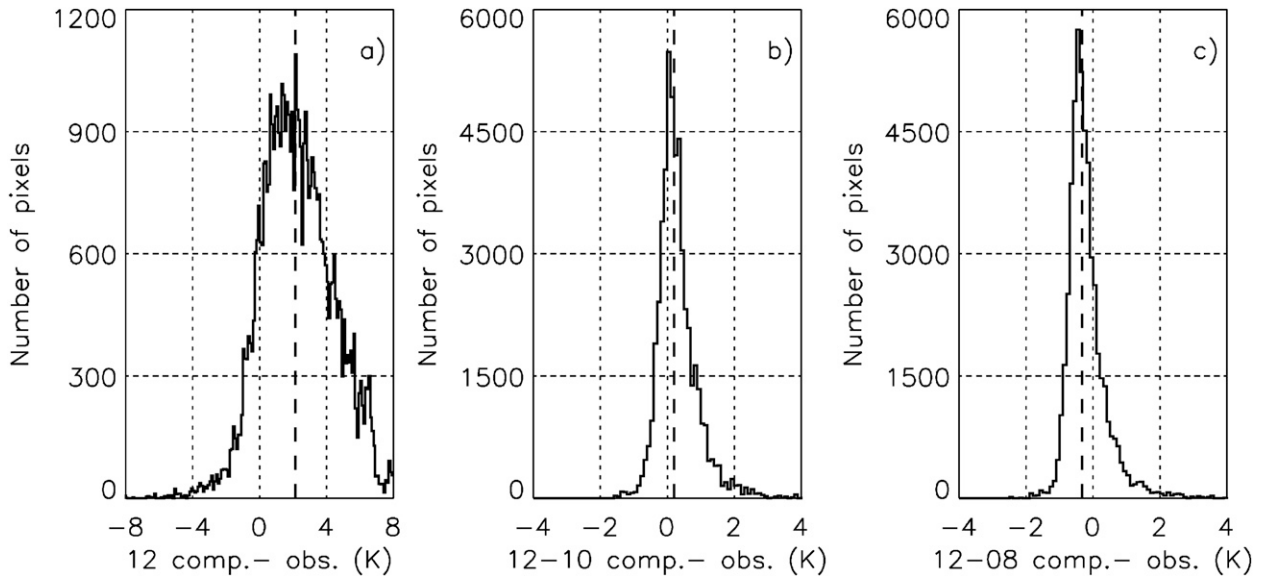


FIG. 6. As in Fig. 4, but for low opaque clouds.

background radiances, the combination of the errors on $\epsilon_{\text{eff},12}$ and $\epsilon_{\text{eff},k}$ leads to the unrealistic interchannel effective emissivity differences seen in Fig. 7a (dashed lines). However, for observed background radiances (solid lines), the median values of $\Delta\epsilon_{12-10}$ and $\Delta\epsilon_{12-08}$ show the expected behavior versus $\epsilon_{\text{eff},12}$, even though a residual bias of -0.004 at $\epsilon_{\text{eff},12} = 0$ is still present, inducing the rapid decrease of $\beta_{\text{eff},12}/k$ seen in Fig. 7b for $\epsilon_{\text{eff},12} < 0.05$. We can see that the impact on the microphysical index 12–8 is very strong, which precludes any accurate retrieval using computed background radiances. This is possibly due to the scattering contribution not accounted for in the determination of the low cloud background radiance using FASRAD. Second-order

corrections should be considered in the next version of the algorithm using tabulated values to maintain a short processing time.

In the following, the discussion is limited to the cases for which the background radiance could be derived from observations rather than from computations. This makes it possible to attempt the microphysical retrievals for clouds of very small emissivity over ocean, as well as over land, and in the case of a semitransparent overlying a low opaque cloud. Consequently, the error $d\Delta\epsilon_{12-k_BG}$ is simulated assuming that the uncertainties $dT_{\text{BG},12}$ and $dT_{\text{BG},k}$ in the brightness temperatures measured at $12.05\ \mu\text{m}$ and in channel k are due to the radiometric noise and are not correlated. As expected, the error

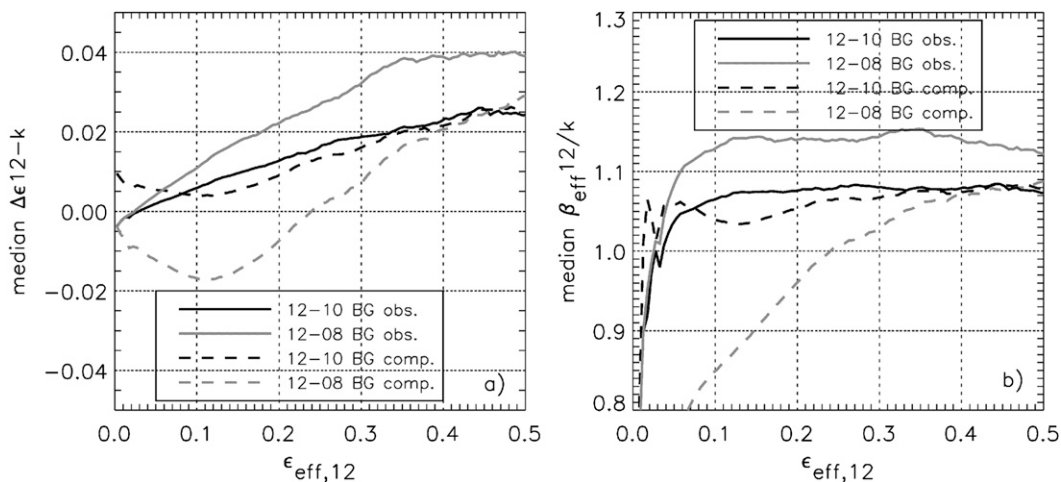


FIG. 7. As in Fig. 5, but for cirrus overlying a low (<7 km) opaque cloud.

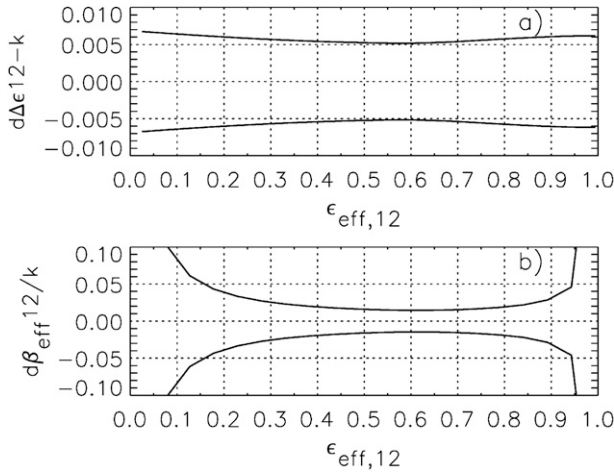


FIG. 8. Overall uncertainty estimates for (a) $d\Delta\epsilon_{12-k}$ and (b) $d\beta_{\text{eff}12/k}$ against $\epsilon_{\text{eff},12}$ for $\beta_{\text{eff}12/k} = 1.1$.

$d\Delta\epsilon_{12-k_BG}$ (see Table 3) decreases as $\epsilon_{\text{eff},12}$ increases. Further studies are needed to improve the accuracy of the computed background radiances for future versions of the algorithm.

3) ERRORS ON THE BLACKBODY RADIANCES

The blackbody radiance $B_k(T_c, Z_c)$ is computed using FASRAD assuming that the equivalent radiative altitude of the cloud Z_c is located at the centroid altitude of the cloud layer as determined by the CALIOP algorithm. The error $d\Delta\epsilon_{12-k_BB}$ [Eq. (9c)] is simulated knowing that the uncertainties $dT_{\text{BB},12}$ and $dT_{\text{BB},k}$ in the blackbody brightness temperatures are not independent, as they are retrieved from FASRAD using the same meteorological data. The interchannel differences mostly depend on the amount of water vapor above the high-altitude cloud derived from the meteorological

data and are typically equal to a few tenths of a kelvin (depending on altitude and latitude, and typically less than 0.3 K for high clouds above 7 km). Also, as mentioned earlier, the computations of the blackbody temperatures with FASRAD do not include multiple scattering. Comparisons with FASDOM, which accounts for multiple scattering, show a good agreement within 0.3 K for effective diameters larger than 10 μm at both 12.05 and 10.6 μm , and for crystal sizes larger than 30 μm at 8.65 μm . However, FASRAD overestimates the 08.65- μm blackbody temperature by about 1 K for sizes of the order of 10 μm . As a result, the microphysical index $\beta_{\text{eff}12/08}$ is in those cases underestimated by about 0.05 at $\epsilon_{\text{eff},12} = 0.9$ and by 0.10 at $\epsilon_{\text{eff},12} = 0.95$. Nevertheless, because of the very large sensitivity of the method for sizes of 10 μm (Fig. 3a), the error on D_e would not exceed a few micrometers. To more extensively quantify this error, calculations have been performed assuming $dT_{\text{BB},12} = \pm 1$ K to include an error on T_c inferred from the equivalent radiative altitude, and with $dT_{\text{BB},12} - dT_{\text{BB},k} = \pm 0.1$ K assuming an error of 30% due to the relative humidity. The resulting error $d\Delta\epsilon_{12-k_BB}$ reported in Table 3 increases with $\epsilon_{\text{eff},12}$, as expected. As the error is further increasing beyond acceptable values at larger emissivities, we will have to limit the analysis domain in the upper range, as will be discussed in next subsection.

4) OVERALL UNCERTAINTY

The overall uncertainty in $\Delta\epsilon_{12-k}$ is computed assuming that the three sources of uncertainty previously discussed are independent, so that the overall error is written

$$d\Delta\epsilon_{12-k} = \sqrt{d\Delta\epsilon_{12-k_m}^2 + d\Delta\epsilon_{12-k_BG}^2 + d\Delta\epsilon_{12-k_BB}^2}. \tag{10}$$

Simulations of $\Delta\epsilon_{12-k}$ derived from Eq. (10) and corresponding errors on $\beta_{\text{eff}12/k}$ are reported in Table 3 and shown in Figs. 8a and 8b, respectively. These estimates are for retrievals at the IIR pixel resolution of 1 km. Even though $d\Delta\epsilon_{12-k}$ vary by less than 40% with $\epsilon_{\text{eff},12}$, $d\beta_{\text{eff}12/k}$ is 3 times larger at small ($\epsilon_{\text{eff},12} = 0.1$) and large ($\epsilon_{\text{eff},12} = 0.96$) effective emissivity than in the medium range ($\epsilon_{\text{eff},12}$ from 0.3 to 0.85), where the estimated random error is ± 0.025 . Indeed, the microphysical index $\beta_{\text{eff}12/k}$ is primarily a measure of the microphysical properties, whereas the variation with $\epsilon_{\text{eff},12}$ of its uncertainty reflects the varying sensitivity of the technique. Nevertheless, the retrievals will be attempted down to

$\epsilon_{\text{eff},12} \sim 0.0$, using measured references, which allows for reducing the errors as discussed earlier. For the largest emissivities, the main unknowns in the error estimates are possible biases in the computation of the blackbody radiances. Indeed, Fig. 5a shows that $\Delta\epsilon_{12-08}$ and $\Delta\epsilon_{12-10}$ do not tend to 0 when $\epsilon_{\text{eff},12}$ tends to 1 but to a residual value of 0.003–0.005. On the other hand, we observe that $\Delta\epsilon_{12-k}$ steadily decreases with increasing $\epsilon_{\text{eff},12}$ as expected, showing a minimum at $\epsilon_{\text{eff},12} = 0.95$. This suggests that $\epsilon_{\text{eff},12}$ is underestimated and should be closer to 1 for this population of clouds. As these clouds typically fully attenuate the CALIOP beam, the centroid altitude Z_c can be too high, T_c too small, and consequently

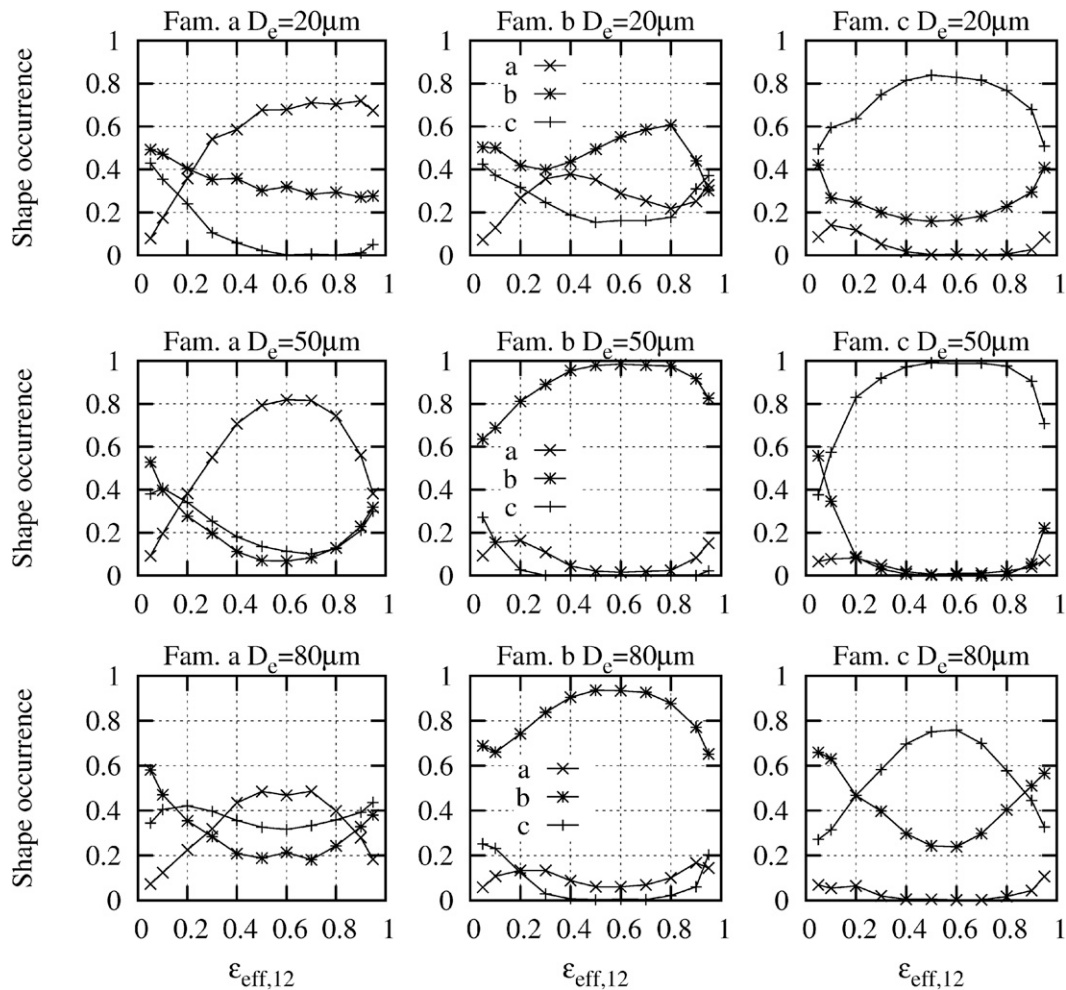


FIG. 9. Impact of a random error on the crystal family selection (a: cross; b: star; and c: plus sign) as a function of the effective emissivity $\epsilon_{\text{eff},12}$ in case of families (left) a (aggregates), (center) b (plates), and (right) c (solid columns) for $D_e =$ (top) 20, (middle) 50, and (bottom) 80 μm .

$\epsilon_{\text{eff},12}$ can be underestimated. There is unfortunately no straightforward consistency check available to the IIR algorithm to accurately assess the errors at very large emissivity. Therefore, we choose to limit the retrievals to $\epsilon_{\text{eff},12}$ smaller than 0.95 where the error on the microphysical indices stays within ± 0.05 according to the simulations.

b. Effective diameter

In this subsection, we present the uncertainty in the retrievals of D_e directly driven by the errors on the microphysical indices and assume that the LUTs have been correctly determined (see discussions in section 3). The IIR algorithm is presently designed to constrain the retrieval by selecting the crystal family that minimizes the difference between $D_{e,12/10}$ and $D_{e,12/08}$ on a 1-km pixel basis. Random errors on the microphysical indices can

direct the algorithm to the wrong crystal family and ultimately to a wrong D_e . Simulations have been performed to assess the errors induced by this artifact for the cases for which the background reference is retrieved from neighboring observations with no bias as discussed in section 4a and with a random noise as shown in Fig. 8. Figure 9 shows the fraction of each crystal family selected for a cloud composed entirely of aggregates (a, left-hand column), plates (b, center), and solid columns (c, right-hand column). The results are shown against the effective emissivity $\epsilon_{\text{eff},12}$ and for “true” D_e equal to 20 μm (top), 50 μm (middle), and 80 μm (bottom). As expected, the selection is the most accurate when the error on the microphysical indices is the smallest, that is, for $\epsilon_{\text{eff},12}$ typically between 0.3 and 0.9. The best scores are obtained for $D_e = 50 \mu\text{m}$ because this range of diameters is where the relationship between

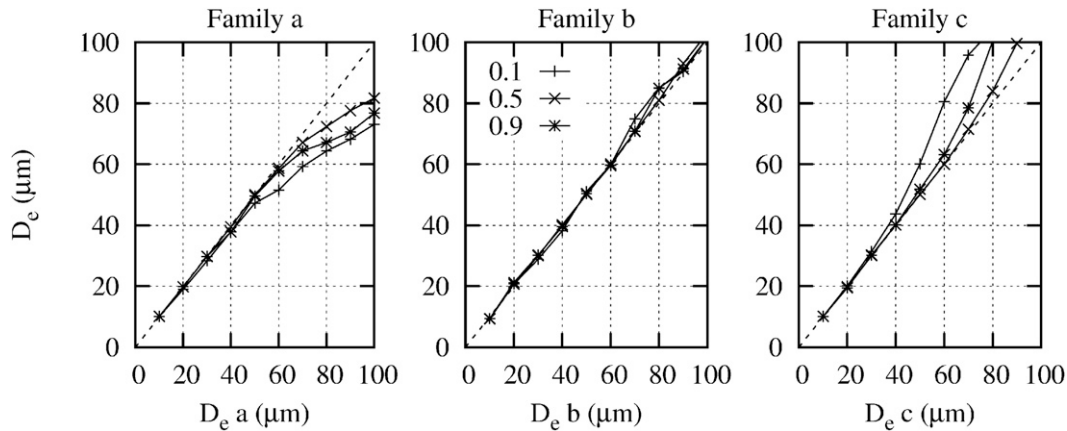


FIG. 10. Impact of the random error and crystal family selection on the median value of D_e (y axis) for a specified D_e (x axis) in family (left) a, (center) b, and (right) c for $\epsilon_{\text{eff},12} = 0.1$ (plus sign), 0.5 (cross), and 0.9 (star).

$\beta_{\text{eff}12/10}$ and $\beta_{\text{eff}12/08}$ differs the most from one model to another, as seen in Fig. 3b. Families b (plates and bullet rosettes) and c (solid columns, droxtals) can be here identified with up to 100% accuracy, whereas a lower score of 80% is obtained for family a (aggregates, hollow columns, and spheroids) whose LUT is located “between” its companions. The best scores are between 60% and 85% for $D_e = 20 \mu\text{m}$ and between 50% and 95% for $80 \mu\text{m}$.

Figure 10 shows the impact on the median D_e (y axis) of the random error and resulting crystal model selection for a simulated cloud composed entirely of aggregates (a, left), plates (b, center), and solid columns (c, right) of specified D_e (x axis). The results are shown for $\epsilon_{\text{eff},12}$ equal to 0.1, 0.5, and 0.9. The simulations show that D_e is correctly retrieved for D_e smaller than $40 \mu\text{m}$ over the full range of effective emissivity and for the three families thanks to the large sensitivity of the method,

which outcores the random errors on the microphysical indices and the erroneous crystal selections. The ability to well classify family b even for large diameters allows a bias smaller than 6% up to $D_e = 100 \mu\text{m}$. For a cloud supposedly composed of solid columns (respectively aggregates), the misclassifications induce a positive (respectively negative) bias. The bias is the largest at $\epsilon_{\text{eff},12} = 0.1$, representing up to 30% (respectively -20%) at $D_e = 80 \mu\text{m}$ for solid columns (respectively aggregates). For $\epsilon_{\text{eff},12} = 0.5$ (respectively 0.9), the bias remains smaller than 10% (respectively 25%) up to $D_e = 80 \mu\text{m}$. The standard deviations associated with the median values shown in Fig. 10 are plotted in Fig. 11. They increase with D_e , as the sensitivity of the method weakens and are much larger at $\epsilon_{\text{eff},12} = 0.1$ than at $\epsilon_{\text{eff},12} = 0.5$ or 0.9 because of the larger errors on the microphysical indices. These results are summarized in Table 4.

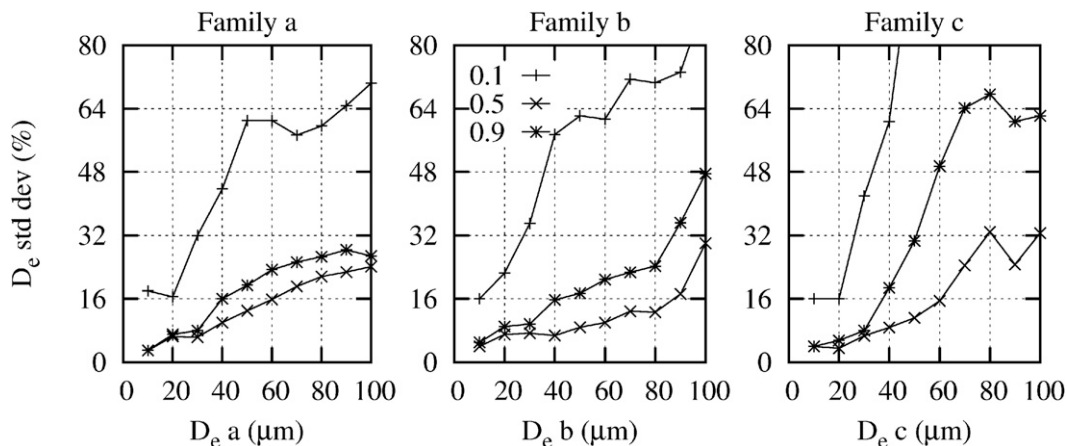


FIG. 11. Simulation of the standard deviation of D_e (%) in case of family (left) a, (center) b, and (right) c for $\epsilon_{\text{eff},12} = 0.1$ (plus sign), 0.5 (cross), and 0.9 (star).

TABLE 4. Values in percent of the effective diameters D_e biases and standard deviations (in parentheses) for given values of D_e and three effective emissivities (0.1, 0.5, and 0.9) for aggregates, plates, and solid columns selected as representative of the families a, b, and c, respectively.

D_e (μm)	Family a			Family b			Family c		
	0.1	0.5	0.9	0.1	0.5	0.9	0.1	0.5	0.9
20	<1% (16)	-1% (6)	-1% (7)	+4% (22)	+3% (7)	<1% (9)	<1% (16)	-1% (3)	-2.5% (6)
40	-5% (44)	-1.2% (10)	-5% (16)	-4% (57)	<1% (7)	-1% (16)	+9% (60)	<1% (9)	<1% (18)
80	-20% (60)	-10% (22)	-16% (27)	+6% (70)	+1% (12)	+6% (24)	+30% (120)	+5% (33)	+25% (68)

5. Results and discussions

a. Effective diameter

The data have been first analyzed for high-altitude (>7 km) semitransparent (ST) single-layered ice cirrus ($T_c < 233$ K) clouds (from type 21 and 30; see G1) over ocean between 60°S and 60°N during January 2011, after selecting the pixels for which the background radiance could be determined from observations, as discussed previously. Figure 12a shows the 2D histogram of the effective diameter $D_e = (D_{e12/08} + D_{e12/10})/2$ as a function of the effective emissivity $\epsilon_{\text{eff},12}$. The differential in D_e due to the averaging of $D_{e12/08}$ and $D_{e12/10}$ is defined as $D_{e_u} = (D_{e12/08} - D_{e12/10})/2$. The 2D histogram of D_{e_u} and $\epsilon_{\text{eff},12}$ is shown in Fig. 12b. The black dots in Figs. 12a and 12b are the median values in each bin of effective emissivity. Figure 12b shows that a good agreement between the two pairs of channels is obtained on average with a median value of D_{e_u} smaller than $1.5 \mu\text{m}$, and a standard deviation of about $8 \mu\text{m}$. The median D_e (Fig. 12a) increases rapidly from 18 to $34 \mu\text{m}$ between $\epsilon_{\text{eff},12} = 0$ and 0.1, then up to $45 \mu\text{m}$ at $\epsilon_{\text{eff},12} = 0.7$.

The observed standard deviation is about $17 \mu\text{m}$ at all emissivities. It includes the contribution of the random errors, whose estimates are 10 – $13 \mu\text{m}$ for $\epsilon_{\text{eff},12} = 0.1$ and $D_e = 30 \mu\text{m}$, decreasing to $4 \mu\text{m}$ for $\epsilon_{\text{eff},12} = 0.5$ and $D_e = 40 \mu\text{m}$ (Fig. 11). The observed standard deviation appears to be larger but consistent with our simulations. This is a fair agreement, keeping in mind the unknown contribution of the natural variability of the cloud microphysical properties, and the limited sampling causing the number of points to decrease as the effective diameter increases. Figure 13 shows the crystal model occurrence corresponding to Fig. 12. The fraction of family c (solid columns and droxtals) is seen to be preponderant. It, however, decreases from 65% at $\epsilon_{\text{eff},12} = 0.1$ to 50% at $\epsilon_{\text{eff},12} = 0.6$, whereas the fraction of family a (aggregates, hollow columns or spheroids) steadily increases from about 15% to 30%. The fraction of family b crystals (plates or bullet rosettes) stays almost constant between 15% and 20%. Comparison of aggregate occurrence as a function of emissivity to results previously reported by Gui12 shows that family a (aggregates and hollow columns) exhibits behavior

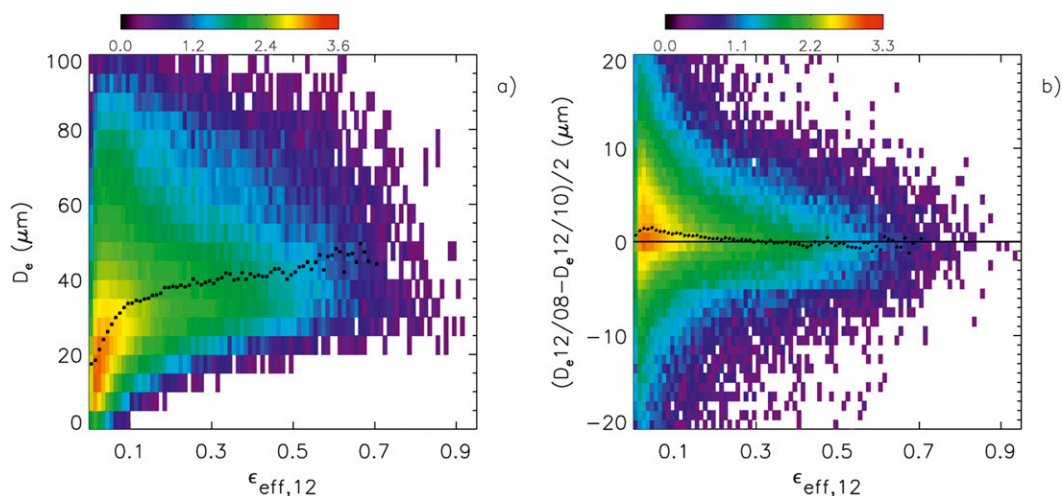


FIG. 12. The 2D histogram of (a) the effective diameter D_e and (b) $D_{e_u} = (D_{e12/08} - D_{e12/10})/2$, and the effective emissivity $\epsilon_{\text{eff},12}$ for high-altitude (>7 km) semitransparent single-layered ice cirrus ($T_c < 233$ K) clouds over ocean between 60°S and 60°N during January 2011. The color code represents the decimal logarithm of the number of points. The superimposed small black dots are the median values in each bin of effective emissivity.

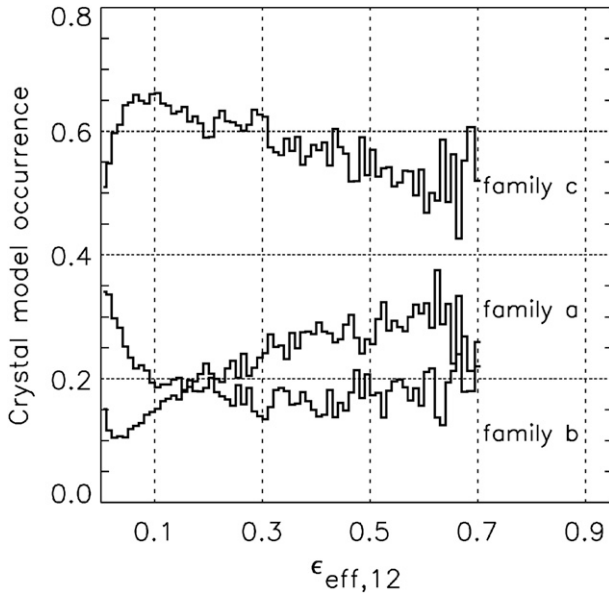


FIG. 13. Occurrence of the crystal families associated with Fig. 12.

similar to a 6-yr climatology from AIRS (Gui12, their Fig. 4). However, the occurrence fractions obtained in our analysis are about half as large. Note that while Gui12 use 6 channels in the 8–12- μm region and more elaborated crystal model assumptions, their cloud detection scheme relies on passive radiometry, leading them to consider only clouds with emissivities larger than 0.2. According to the simulations in Fig. 9 for aggregates and $D_e = 20$ or $50 \mu\text{m}$, random errors could

introduce a low bias in the aggregate-like shape occurrence as $\epsilon_{\text{eff},12}$ decreases. Nevertheless, no significant bias of the median D_e is to be expected because of erroneous aggregate shape detection as D_e is in the range of 20–40 μm where simulations indicate a limited impact of the crystal model selected (Fig. 10).

The previous analysis for January 2011 over ocean has been extended over land, and for cirrus clouds overlying a low opaque cloud, to analyze cirrus clouds associated with different categories of background radiances. The results are reported in Fig. 14a for the effective diameter and Fig. 14b for the crystal type occurrence of families a and c. In addition, clouds classified as ST (thin lines) and opaque (thick lines) by CALIOP are distinguished. The crystal model occurrence is remarkably close for the three families of ST clouds with differences of less than 10% at low emissivity. For the opaque clouds fully attenuating the CALIOP laser beam (type 40 in G1), the solid columns occurrence increases from 0.6 to 0.8 for $\epsilon_{\text{eff},12}$ greater than 0.8 both over sea and over land. The median effective diameters are similar for the three families of ST clouds, within 2–3 μm for medium emissivities $\epsilon_{\text{eff},12} \sim 0.5$ –0.6. We observe an excellent agreement between opaque and ST clouds over sea in the overlapping range of $\epsilon_{\text{eff},12}$ between 0.5 and 0.7. For opaque clouds, D_e increases rapidly by 10 μm from $\epsilon_{\text{eff},12} = 0.8$ up to about 60 μm at $\epsilon_{\text{eff},12} = 0.95$, D_e being lower over land than over sea, by about 5 μm at $\epsilon_{\text{eff},12} = 0.95$, whereas the crystal model occurrences are identical. As these differences are seen in the larger range of emissivity, they cannot be attributed to an artifact linked

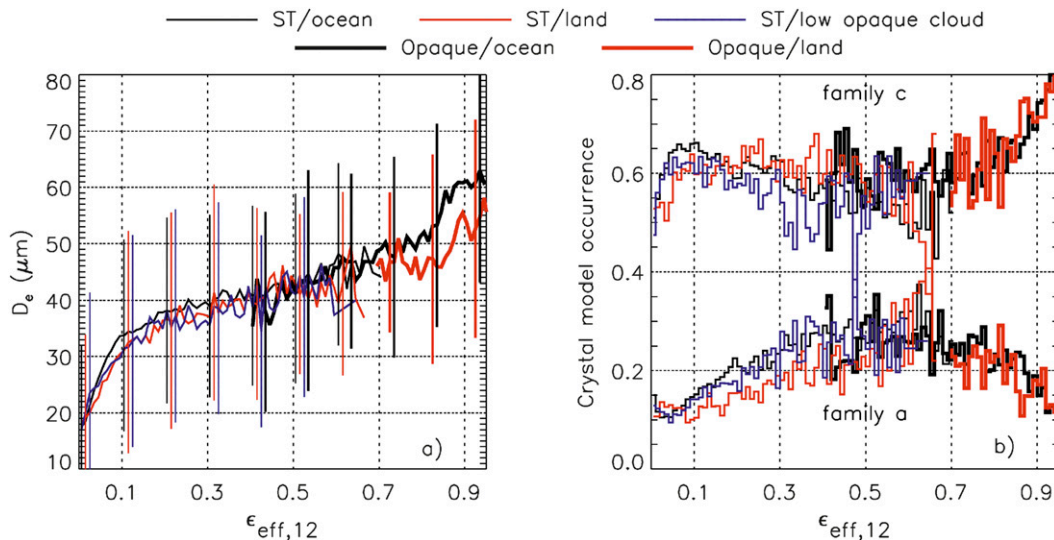


FIG. 14. (a) Median effective diameter ± 1 standard deviation and (b) crystal model occurrence vs $\epsilon_{\text{eff},12}$ for high-altitude ($>7 \text{ km}$) single-layered ice cirrus ($T_c < 233 \text{ K}$) clouds between 60°S and 60°N over ocean (black), land (red), and low opaque clouds (blue) during January 2011. Thin and thick lines are for ST and opaque clouds, respectively.

to the background radiance retrievals (see section 4) and can be considered as real, notwithstanding the standard deviation of the order of $20\ \mu\text{m}$. Gui12 also observe a similar increase of D_e with $\varepsilon_{\text{eff},12}$ (see their Fig. 4), but with a larger slope at middle emissivity, for example $+10\%$ – 30% (50 – $60\ \mu\text{m}$) at $\varepsilon_{\text{eff},12} \sim 0.6$, and with D_e rapidly decreasing for emissivities larger than 0.85 , behavior that is not observed here. Wang et al. (2011) find crystal diameters in the same range of values as in our study by using a new fast radiative transfer model applied to similar MODIS channels.

b. Ice water path and ice water content

Parameterizations linking ice clouds microphysical and optical properties for implementation in large-scale models have been proposed by several authors. The IIR data provide independent retrieval of optical depth and effective diameter, as the latter is derived from the pairs of microphysical indices, shown not to vary significantly with effective emissivity. The cloud-layer ice water path is inferred from the optical depth and the effective particle diameter, using relationships discussed in section 2. More interestingly, to take advantage of the cloud boundaries simultaneously derived by CALIOP, we have chosen to discuss here the mean ice water content (IWC) as derived from the IWP divided by the cloud thickness and the mean layer extinction coefficient α , which can be estimated from $2 \times \text{OD}_{\text{eff}}$ divided by the cloud thickness. As given in section 2, the effective diameter can be expressed as the ratio between the mean IWC and the mean extinction coefficient. Equation (2) can thus be rewritten

$$D_e = 3.27 \times \frac{\text{IWC}}{\alpha}, \quad (11)$$

where D_e is in micrometers, IWC is in grams per meter cubed, and α is in inverse meters. We choose to analyze our retrievals in terms of relationship between D_e and extinction, and the resulting relationship between IWC and extinction. The median D_e is shown in Fig. 15 against α inferred from the IIR for high-altitude ($>7\ \text{km}$) single-layered ST (thin lines) and opaque (thick line) ice cirrus clouds over ocean during January 2011. The results are shown for various temperature ranges: $T_c < 203\ \text{K}$ (navy blue), T_c in 203 – $213\ \text{K}$ (light blue), 213 – $223\ \text{K}$ (green), and 223 – $233\ \text{K}$ (red), for which the fraction of ST clouds is 11% , 17% , 35% , and 37% , respectively. Opaque clouds are found mostly at 213 – $223\ \text{K}$ (34%) and 223 – $233\ \text{K}$ (60%). The standard deviation (not shown) is 15 – $20\ \mu\text{m}$. The geometrical thickness is prevalingly between 0.5 and $2\ \text{km}$ for the ST clouds with extinctions smaller than $0.001\ \text{m}^{-1}$. For

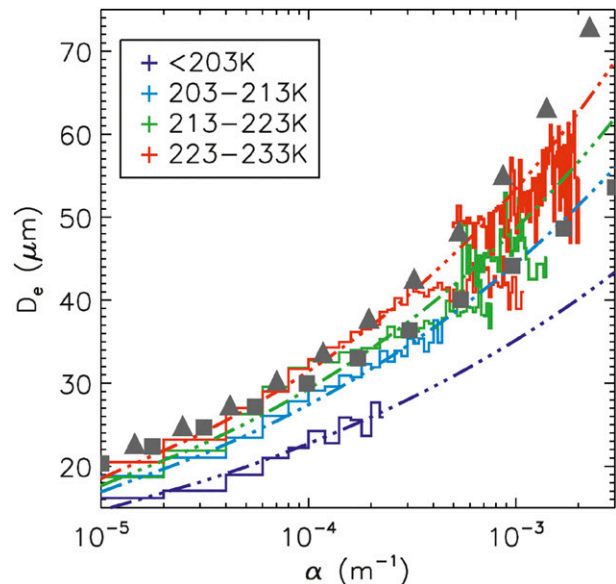


FIG. 15. Median effective diameter vs extinction coefficient for high-altitude ($>7\ \text{km}$) single-layered ST (thin line) and opaque (thick line) ice cirrus clouds over ocean during January 2011 for $T_c < 203\ \text{K}$ (navy blue), T_c between 203 – $213\ \text{K}$ (light blue), 213 – $223\ \text{K}$ (green), and 223 – $233\ \text{K}$ (red). The squares are from M10 and the triangles are from McF03. The dash-dotted color lines are best fits derived from this study.

opaque clouds, the thickness is found to be mainly between 1 and $3\ \text{km}$, but these values are likely underestimated as such clouds totally attenuate the laser beam. It is seen in Fig. 15 that D_e increases with α and temperature, between 16 and $45\ \mu\text{m}$ for ST clouds, and is larger for opaque clouds, up to $60\ \mu\text{m}$ at 223 – $233\ \text{K}$, with a fairly good overlap. A more rapid increase of D_e with α cannot be ruled out for opaque clouds, as α could be overestimated. The 2D histogram of IWC and α corresponding to Fig. 15 is shown in Fig. 16, for all temperatures and extinction coefficients larger than $10^{-4}\ \text{m}^{-1}$. The median IWC/ α ratio is between 5 ± 4.6 and $14 \pm 7\ \text{g m}^{-2}$ for ST clouds, up to $18 \pm 7\ \text{g m}^{-2}$ for opaque clouds. The IIR D_e retrievals can be further compared with in situ measurements of the IWC/ α ratio available in the literature. The squares in Figs. 15 and 16 show the relationship derived from in situ measurements at midlatitude by Mioche et al. (2010, hereinafter M10) who proposed a relationship between IWC and α of

$$\text{IWC} = 44\alpha^{1.17}, \quad (12)$$

whereas the triangles show the “base case” results from McF03 in the tropics. Our results, representing a global average, agree well with both in situ results for temperatures between 213 and $233\ \text{K}$. Interestingly, power-law relationships between IWC and α can also be obtained

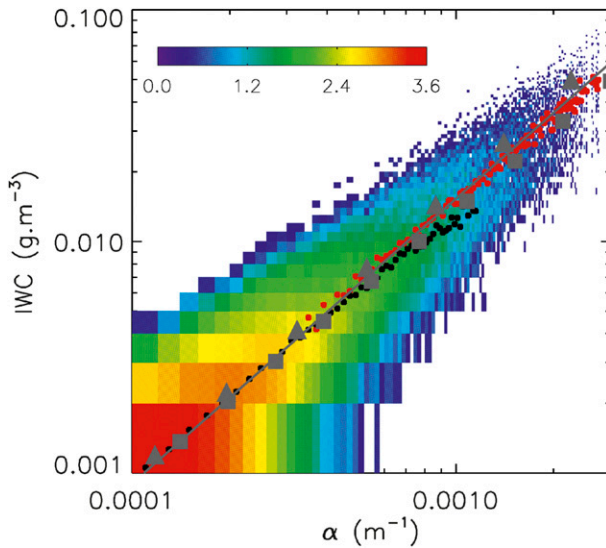


FIG. 16. The 2D histogram of ice water content and extinction coefficient for high-altitude (>7 km) single-layered ST and opaque ice cirrus clouds over sea during January 2011 for $T_c < 233$ K. The color code represents the decimal logarithm of the number of points. Superimposed in black and red are the median values in each bin of extinction for the ST and opaque clouds, respectively. The squares are from M10 and the triangles from McF03. The gray solid line is the best fit derived from this study.

from the IIR for the four ranges of temperature using the coefficients reported in Table 5 (dash-dotted colored lines in Fig. 15). The IIR median D_e increases more rapidly with α than in M10, more in agreement with McF03. Considering that tropical latitudes have more cirrus than midlatitudes and that the largest extinction coefficients in opaque clouds may be overestimated reconciles these results. Average coefficients characterizing the whole global cloud population (solid curve in Fig. 16) derived using the same power-law relationship are $a = 75$ and $b = 1.23$.

Overall, these results show a good consistency between the IIR microphysics retrievals and knowledge established from in situ observations only (M10) or including remote sensing measurements from the Atmospheric Radiation Measurement sites (McF03). However, the effective diameters and IWC reported in this study are lower by about 40% than those reported by Heymsfield et al. (2005).

6. Conclusions

The results presented in this paper have been obtained with the version-3 IIR level-2 operational algorithm for the retrieval of cirrus clouds' effective diameters and ice water path, whose definitions are presented and discussed. The analysis relies on two effective microphysical indices defined as the ratio of the effective optical depths for the pairs of channels (12.05, 10.6) and (12.05, 08.65) and uses a series of LUTs computed offline by using the FASDOM model. Three crystal families representative of main relationships between the microphysical indices are chosen from a precomputed database. The effective diameter is inferred from the crystal family that best simulates the pair of retrieved microphysical indices, assuming a monodisperse size distribution. Errors of about 15%–20% on the effective diameters due to these simplifications have been discussed. The impact of the microphysical index random error on the crystal model selection and the effective diameters retrievals has been simulated. The possible biases have been assessed through consistency checks based on effective emissivity differences. It has been shown that the retrievals of single-layered cirrus clouds can be attempted, for the first time, down to effective emissivities close to 0.05 when accurate measured background radiances can be used to reduce biases due to ancillary parameters and radiative calculations, and up to 0.95 where errors due to blackbody radiance become significant. An excellent consistency between retrievals over ocean, over land, and in the case of clouds overlying a low opaque cloud, as well as between ST and opaque clouds, has been found in terms of both crystal model selection and effective diameter. For high-altitude single-layered cirrus clouds with centroid temperature smaller than 233 K during January 2011, solid columns (family c) are selected in 60% of the cases on average for ST clouds, increasing up to 80% in opaque clouds. The median effective diameters increase with effective emissivity between 18 and 60 μm for effective emissivities from 0.05 to 0.95. The standard deviations are $\pm 17 \mu\text{m}$ on average, larger but still compatible with the simulations, since they include the natural variability. The relation between median effective diameter or IWC and mean

TABLE 5. Coefficients a and b used to link IWC (g m^{-3}) and extinction coefficient α (m^{-1}) through the power-law relationship $\text{IWC} = a\alpha^b$.

T_c	IIR, January 2011, ocean, single-layer clouds, altitude > 7 km					M10
	<203 K	203–213 K	213–223 K	223–233 K	All	
ST clouds	11%	17%	35%	37%	100%	
Opaque clouds	0.5%	5.5%	34%	60%	100%	
a	40	58	68	80	75	44
b	1.19	1.21	1.22	1.23	1.23	1.17

extinction shows a good agreement with the relationship established by in situ observations at midlatitudes (M10) and tropical latitudes (McF03). An IIR power-law relationship between IWC and extinction was established for four temperature ranges for the dataset presented in this paper. An average global relationship is also given that presents a simpler approach for large-scale models.

Overall, these results indicate accurate retrievals of the microphysical indices down to very small and up to rather large effective emissivity, notwithstanding the random noise, because this is partly compensated by the sensitivity of the method to particles with small diameters of several tens of micrometers. The perfectly collocated vertical information provided by the CALIOP lidar and the resulting accurate knowledge of the background conditions in each IIR channel are the main drivers of these performances. Future work will include an improved modeling of the background computed radiances for both clear and cloudy cases and an improved determination of blackbody radiance to improve retrievals at large emissivity, and thus increase the range in cloudy conditions of the data. Studies will be conducted for a refined selection of the LUTs and for the use of temperature and depolarization ratio from CALIOP as an additional constraint to better identify the relevant crystal model.

Acknowledgments. The authors thank F. Parol, C. Stubenrauch, and S. Ackerman for fruitful discussions, the ICARE data center, and the CALIPSO team at NASA Langley Research Center for their help with the IIR level-2 algorithm. The products are processed at NASA/LARC and are publicly available at NASA/LARC (<https://eosweb.larc.nasa.gov/>) and ICARE (<http://www.icare.univ-lille1.fr/>) data centers. The authors are thankful to CNES, Centre National de la Recherche Scientifique (CNRS), Institut National des Sciences de l'Univers (INSU), and NASA for their support.

REFERENCES

- Ackerman, S. A., W. L. Smith, J. D. Spinhirne, and H. E. Revercomb, 1990: The 27–28 October 1986 FIRE IFO cirrus case study: Spectral properties of cirrus clouds in the 8–12 μm window. *Mon. Wea. Rev.*, **118**, 2377–2388.
- , —, A. D. Collard, X. L. Ma, H. E. Revercomb, and R. O. Knuteson, 1995: Cirrus cloud properties derived from High Spectral Resolution Infrared Spectrometry during FIRE II. Part II: Aircraft HIS results. *J. Atmos. Sci.*, **52**, 4246–4263.
- Bugliaro, L., T. Zinner, C. Keil, B. Mayer, R. Hollmann, M. Reuter, and W. Thomas, 2011: Validation of cloud property retrievals with simulated satellite radiances: A case study for SEVIRI. *Atmos. Chem. Phys.*, **11**, 5603–5624, doi:10.5194/acp-11-5603-2011.
- Chiriaco, M., H. Chepfer, V. Noel, A. Delaval, M. Haeffelin, P. Dubuisson, and P. Yang, 2004: Improving retrievals of cirrus cloud particle size coupling lidar and three-channel radiometric techniques. *Mon. Wea. Rev.*, **132**, 1684–1700.
- Corlay, G., M.-C. Arnolfo, T. Bret-Dibat, A. Lifermann, and J. Pelon, 2000: The Infrared Imaging Radiometer for PICASSO-CENA., CNES Tech. Doc., 14 pp. [Available online at http://smc.cnes.fr/CALIPSO/IIR_ICSO00_S2-06.pdf.]
- Dubuisson, P., V. Giraud, O. Chomette, H. Chepfer, and J. Pelon, 2005: Fast radiative transfer modeling for infrared imaging radiometry. *J. Quant. Spectrosc. Radiat. Transfer*, **95** (2), 201–220.
- , —, J. Pelon, B. Cadet, and P. Yang, 2008: Sensitivity of thermal infrared radiation at the top of the atmosphere and the surface to ice cloud microphysics. *J. Appl. Meteor. Climatol.*, **47**, 2545–2560.
- Duda, D. P., J. D. Spinhirne, and W. D. Hart, 1998: Retrieval of contrail microphysical properties during SUCCESS by the split-window method. *Geophys. Res. Lett.*, **25**, 1149–1152.
- Ebert, E. E., and J. A. Curry, 1992: A parameterization of ice cloud optical properties for climate models. *J. Geophys. Res.*, **97** (D4), 3831–3836.
- Fu, Q., 1996: An accurate parameterization of the solar radiative properties of cirrus clouds for climate models. *J. Climate*, **9**, 2058–2082.
- , and K. N. Liou, 1993: Parameterization of the radiative properties of cirrus clouds. *J. Atmos. Sci.*, **50**, 2008–2025.
- , P. Yang, and W. B. Sun, 1998: An accurate parameterization of the infrared radiative properties of cirrus clouds for climate models. *J. Climate*, **11**, 2223–2237.
- Garnier, A., J. Pelon, P. Dubuisson, M. Faivre, O. Chomette, N. Pascal, and D. P. Kratz, 2012: Retrieval of cloud properties using CALIPSO Imaging Infrared Radiometer. Part I: Effective emissivity and optical depth. *J. Appl. Meteor. Climatol.*, **51**, 1407–1425.
- Giraud, V., J. C. Buriez, Y. Fouquart, F. Parol, and G. Sèze, 1997: Large-scale analysis of cirrus clouds from AVHRR data: Assessment of both a microphysical index and the cloud-top temperature. *J. Appl. Meteor.*, **36**, 664–675.
- Guignard, A., C. J. Stubenrauch, A. J. Baran, and R. Armante, 2012: Bulk microphysical properties of semi-transparent cirrus from AIRS: A six year global climatology and statistical analysis in synergy with geometrical profiling data from CloudSat-CALIPSO. *Atmos. Chem. Phys.*, **12**, 503–525, doi:10.5194/acp-12-503-2012.
- Heidinger, A. K., and M. J. Pavolonis, 2009: Gazing at cirrus clouds for 25 years through a split window. Part I: Methodology. *J. Appl. Meteor. Climatol.*, **48**, 1100–1116.
- , —, R. E. Holz, B. A. Baum, and S. Berthier, 2010: Using CALIPSO to explore the sensitivity to cirrus height in the infrared observations from NPOESS/VIIRS and GOES-R/ABI. *J. Geophys. Res.*, **115**, D00H20, doi:10.1029/2009JD012152.
- Heymsfield, A. J., S. Matrosov, and B. Baum, 2003: Ice water path-optical depth relationships for cirrus and deep stratiform ice cloud layers. *J. Appl. Meteor.*, **42**, 1369–1390.
- , D. Winker, and G.-J. van Zadelhoff, 2005: Extinction-ice water content-effective radius algorithms for CALIPSO. *Geophys. Res. Lett.*, **32**, L10807, doi:10.1029/2005GL022742.
- Inoue, T., 1985: On the temperature and effective emissivity determination of semitransparent cirrus clouds by bi-spectral measurements in the 10- μm window region. *J. Meteor. Soc. Japan*, **63**, 88–98.

- McFarquhar, G. M., S. Iacobellis, and R. C. J. Somerville, 2003: SCM simulations of tropical ice clouds using observationally based parameterizations of microphysics. *J. Climate*, **16**, 1643–1664.
- Mioche, G., D. Josset, J.-F. Gayet, J. Pelon, A. Garnier, A. Minikin, and A. Schwarzenboeck, 2010: Validation of the CALIPSO-CALIOP extinction coefficients from in situ observations in midlatitude cirrus clouds during the CIRCLE-2 experiment. *J. Geophys. Res.*, **115**, D00H25, doi:10.1029/2009JD012376.
- Mitchell, D. L., 2002: Effective diameter in radiation transfer: General definition, applications, and limitations. *J. Atmos. Sci.*, **59**, 2330–2346.
- Nakajima, T., and M. D. King, 1990: Determination of the optical thickness and effective particle radius of clouds from reflected solar radiation measurements. Part I: Theory. *J. Atmos. Sci.*, **47**, 1878–1893.
- Parol, F., J. C. Buriez, G. Brogniez, and Y. Fouquart, 1991: Information content of AVHRR channels 4 and 5 with respect to the effective radius of cirrus cloud particles. *J. Appl. Meteor.*, **30**, 973–984.
- Pavolonis, M. J., 2010: Advances in extracting cloud composition information from spaceborne infrared radiances—A robust alternative to brightness temperatures. Part I: Theory. *J. Appl. Meteor. Climatol.*, **49**, 1992–2012.
- Platnick, S., M. D. King, S. A. Ackerman, W. P. Menzel, B. A. Baum, J. C. Riedi, and R. A. Frey, 2003: The MODIS cloud products: Algorithms and examples from Terra. *IEEE Trans. Geosci. Remote Sens.*, **41**, 459–473.
- Pruppacher, H. R., and J. D. Klett, 1997: *Microphysics of Clouds and Precipitation*. Kluwer Academic, 954 pp.
- Rädcl, G., C. J. Stubenrauch, R. Holz, and D. L. Mitchell, 2003: Retrieval of effective ice crystal size in the infrared: Sensitivity study and global measurements from TIROS-N Operational Vertical Sounder. *J. Geophys. Res.*, **108**, 4281, doi:10.1029/2002JD002801.
- Roebeling, R. A., A. J. Feijt, and P. Stammes, 2006: Cloud property retrievals for climate monitoring: implications of differences between Spinning Enhanced Visible and Infrared Imager (SEVIRI) on *Meteosat-8* and Advanced Very High Resolution Radiometer (AVHRR) on *NOAA-17*. *J. Geophys. Res.*, **111**, D20210, doi:10.1029/2005JD006990.
- Sourdeval, O., and Coauthors, 2012: Validation of IIR/CALIPSO level 1 measurements by comparison with collocated airborne observations during CIRCLE-2 and Biscay '08 campaigns. *J. Atmos. Oceanic Technol.*, **29**, 653–667.
- Stephens, G. L., 1978: Radiation profiles in extended water clouds. II: Parameterization schemes. *J. Atmos. Sci.*, **35**, 2123–2132.
- Stubenrauch, C. J., R. Holz, A. Chédin, D. L. Mitchell, and A. J. Baran, 1999: Retrieval of cirrus ice crystal sizes from 8.3 and 11.1 μm emissivities determined by the improved initialization inversion of TIROS-N Operational Vertical Sounder observations. *J. Geophys. Res.*, **104** (D24), 31 793–31 808.
- , S. Cros, A. Guignard, and N. Lamquin, 2010: A 6-year global cloud climatology from the Atmospheric InfraRed Sounder AIRS and a statistical analysis in synergy with CALIPSO and CloudSat. *Atmos. Chem. Phys.*, **10**, 7197–7214.
- Wang, C., P. Yang, B. A. Baum, S. Platnick, A. K. Heidinger, Y. Hu, and R. E. Holz, 2011: Retrieval of ice cloud optical thickness and effective particle size using a fast infrared radiative transfer model. *J. Appl. Meteor. Climatol.*, **50**, 2283–2297.
- Warren, S. G., 1984: Optical constants of ice from the ultraviolet to the microwave. *Appl. Opt.*, **23**, 1206–1225.
- , and R. E. Brandt, 2008: Optical constants of ice from the ultraviolet to the microwave: A revised compilation. *J. Geophys. Res.*, **113**, D14220, doi:10.1029/2007JD009744.
- Yang, P., H. Wei, H. L. Huang, B. A. Baum, Y. X. Hu, G. W. Kattawar, M. I. Mishchenko, and Q. Fu, 2005: Scattering and absorption property database for non-spherical ice particles in the near-through far-infrared spectral region. *Appl. Opt.*, **44**, 5512–5523.
- Yue, Q., K. N. Liou, S. C. Ou, B. H. Kahn, P. Yang, and G. G. Mace, 2007: Interpretation of AIRS data in thin cirrus atmospheres based on a fast radiative transfer model. *J. Atmos. Sci.*, **64**, 3827–3842.